https://doi.org/10.1016/j.biomaterials.2018.04.037

Non-invasive Through-skull Brain Vascular Imaging and Small Tumor Diagnosis Based on NIR-II emissive Lanthanide Nanoprobes Beyond 1500 nm

Zhenluan Xue,[a] *Songjun Zeng*[a,]* *and Jianhua Hao*[b,]*

[a]College of Physics and Information Science and Key Laboratory of Low-dimensional Quantum Structures and Quantum Control of the Ministry of Education, Synergetic Innovation Center for Quantum Effects and Applications, Hunan Normal University, Changsha, Hunan 410081 (China)

[b]Department of Applied Physics, The Hong Kong Polytechnic University, Hong Kong (China)

---

* Address correspondence to songjunz@hunnu.edu.cn; jh.hao@polyu.edu.hk

ABSTRACT

Optical bioimaging by using the new short-wavelength infrared window (SWIR, also named as NIR-II, 1000-1700 nm) is emerged as a next generation imaging technique for disease diagnosis owing to the unprecedented improvements in imaging sensitivity and spatial resolution. However, it is challenging to search new imaging agents with highly biocompatible and bright narrow emission located in the 1500-1700 nm (referred as NIR-IIb) region. Here we developed high quality polyacrylic acid (PAA) modified $NaYF_4$:Gd/Yb/Er nanorods (PAA-NRs) with remarkably enhanced NIR-IIb emission and decent bio-compatibility for *in vivo* cerebral vascular bioimaging and small tumor visualization. These PAA-NRs present efficient narrow-band NIR-IIb emission centered at 1520 with 182 nm of band-width. Owing to the highly efficient NIR-IIb emission, NIR-IIb imaging-guided small tumor (4 mm in diameter) detection is achieved. More importantly, non-invasive optical brain vessel bioimaging with high spatial (~43.65 μm) and temporal resolution through scalp and skull is obtained without craniotomy. These findings open up the opportunity of designing non-invasive approach for visualization the brain vasculature and tumor in biomedical application.

KEYWORDS: Rare-earth doped nanophosphors, Short-wavelength infrared window, Vascular optical imaging, Tumor detection, Dynamic contrast imaging

1. Introduction

In recent years, angiography technologies have achieved great attention because of their providing vascular structure and function information for prognosis, diagnosis and analysis pathological states [1-4]. Vascular imaging based on X-ray computed tomography and magnetic resonance angiography is capable of offering deep-tissue penetration imaging of the vasculature [5,6]. However, these methods still need to be optimized for extracting more comprehensive information due to long scanning times and low sensitivity/spatial resolution [7,8]. Interestingly, fluorescence-based optical imaging method presents attractive features of radiation free, quick feedback, high sensitivity and resolution, leading to more comprehensively structural features of vessel [3,4,9-13]. Therefore, it is urgently demanded to design fluorescence agents for optical vessel imaging.

Present studies on fluorescence agents were mainly focused on emissions located at visible (400-650 nm) or first near-infrared (NIR-I, 650-950 nm, “biological transparency window”) regions [14]. Unfortunately, the wavelength in these regions will bring about strong scattering of biological tissues or organs, subsequently resulting in limited penetration depth with high resolution. Recently, optical imaging by using a new “tissue-transparent window” named as the second NIR region (NIR-II, 1000-1700 nm) holds the merits of 1000-fold reduction in scattering losses than NIR-I region [15-17], leading to a remarkable improvement in imaging resolution and sensitivity, which is considered as the next generation advanced optical imaging method [18-24]. Thus, developing high performance NIR-II-emitting probes have great promising applications for vessel imaging, disease diagnosis and tumor detection. So far, fluorophores capable of emitting NIR-II luminescence such as semiconducting quantum dots (QDs)

[25-29], single-walled carbon nanotubes (SWNTs) [4,18,30-32], and small organic molecules have been developed for NIR-II optical bioimaging [33]. However, most of QDs, such as PbSe, PbS, and CdHgTe, suffer from potential toxicity of heavy metals, resulting in undesirable application for bioimaging [34-36]. Dai's group performed a pioneering study for NIR-II bioimaging by using SWNTs as imaging agents [4,30,37,38]. However, relatively low quantum yield, short excitation wavelength (located at 650 nm), broad emission peaks (>300 nm) and large length distributions of SWNTs ultimately impede their widespread applications in NIR-II imaging. Small organic molecules retain in body too short to accumulate in tumor region, which may hinder their applications in tumor detection and *in vivo* long-term studies that usually need a long time period up to several days [33]. Therefore, it is important to design fluorescent agents with high bio-compatibility, narrow emission, uniform size and high fluorescence quantum yield for *in vivo* NIR-II optical bioimaging.

Rare-earth based nanomaterials were commonly used as optimal nanoprobes for ultrasensitive biodetection and highly sensitive bioimaging due to the outstanding visible and NIR-I upconversion luminescent properties [39]. Compared with the aforementioned fluorescent agents, rare-earth doped nanoprobes possess superior physicochemichal features, such as longer luminescence lifetimes, higher photochemical stability, lower photo-bleaching, larger anti-Stokes shifts, lower autofluorescence, higher penetration depth, higher efficiency, lower long-term cytotoxicity and multi-excitation features [17,40-44]. However, the low quantum yield of visible/NIR-I upconversion emission of rare-earth doped nanomaterials impedes their applications in high sensitive imaging [45]. Fortunately, apart from the upconversion emission, the rare-earth doped nanomaterials also present high efficiency downconversion NIR-II emission with remarkably reduced scattering losses than visible/NIR-I upconversion emission, which is always ignored for bioimaging. Additionally, NIR-II region can be divided into two parts, including NIR-IIa (1000-1400 nm) and NIR-IIb (1500-1700 nm) imaging windows [12]. Nanoprobes employed in NIR-IIb are more superior for *in vivo* imaging, owing to deeper tissue penetration depths, higher spatial and temporal resolution and lower scattering in this region. Although some kinds of rare-earth doped nanomaterials in the NIR-II region have been developed, the application of these probes for NIR-II imaging is still at nascent stage [46-51]. Rare-earth based nanoprobes for *in vivo* fast vascular imaging with high spatial and temporal resolution are still very limited. Therefore, it is vital to search and synthesize high-performance rare-earth doped nanoprobes with NIR-IIb emission for *in vivo* vascular imaging.

In this work, $NaYF_4$:Gd/Yb/Er NRs doped with different Yb^{3+} levels were synthesized under hydrothermal route using oleic acid (OA) as capping agent. Yb-doping induced downconversion NIR-IIb emission enhancement was studied. The toxicity assessment of the polyacrylic acid (PAA) modified NRs (PAA-NRs) was carried out. The PAA-NRs were successfully applied as nanoprobes for *in vivo* NIR-IIb optical bioimaing, optical imaging-guided tiny tumor detection, and non-invasive brain vessel imaging.

2. Materials and methods

2.1. Materials

$YbCl_3$ $6H_2O$(99.9%), YCl_3 $6H_2O$(99.9%), $ErCl_3$ $6H_2O$(99.9%), and $GdCl_3$ $6H_2O$(99.9%) were purchased from Sigma-Aldrich. PAA (Mw: 1800), NaOH, diethylene glycol (DEG), NaF, anhydrous alcohol, OA, toluene, cyclohexane, 1,2-dichloroethane (DCE), IR-26 dye, chloroform and other reagents were analytically pure and obtained from Sinopharm Chemical Reagent Co., China. All chemicals were used without further purification.

2.2. Synthesis of OA-coated NRs

$NaYF_4$:40%Gd/xYb/2%Er (x=10%, 20%, 30%) NRs were synthesized via a hydrothermal route using OA as capping ligand. In a typical procedure [52], 1.2 g NaOH was dissolved in 2 mL deionized water with vigorous stirring to form a clear solution. Anhydrous alcohol (10 mL) and OA (20 mL) were then added to the above solution and stirred for several minutes. A total of 1 mmol of RE $6H_2O$ (RE=Gd, Y, Yb, Er) at a designed molar ratio and 8 mmol of NaF solutions were added to the aforementioned solution under vigorously stirring. Subsequently, the obtained solution was sealed to a Teflon-lined stainless-steel autoclave (50 mL) and heated at 190 °C for 24 h. The resulting precipitates were washed with ethanol and deionized water.

2.3. Synthesis of PAA-NRs

For good bio-compatibility in *in vivo* bioimaging, PAA was used to modify the surface of the OA-NRs as previously reported [53]. Typically, DEG (30 mL) and PAA-1800 (300 mg) were added into a 100 mL flask. Under argon protection, the mixture was heated to 110 °C with vigorously magnetic stirring to form a clear solution. Subsequently, the 100 mg OA-NRs dispersed in cyclohexane were mixed with toluene and then was slowly injected the above solution, the system was protected by argon atmosphere and kept at 110 °C for 1 h. Then the mixed solution was slowly heated to 240 and lasted for 1.5 h. After cooling, the PAA-NRs were collected by centrifugation and were washed with ethanol/ deionized water several times.

2.4. Characterizations

Powder X-ray diffraction (XRD) patterns of samples were tested by a Bruker D8 Discovery diffractometer operating at 40 kV and 40 mA with Cu Kα radiation (λ=1.54056 Å). Morphology of NRs was characterized by field emission transmission electron microscopy (TEM) (FEI Tecnai F20) with an accelerating voltage of 200 kV. Energy-dispersive X-ray spectrometer (EDS) analysis was carried out during high resolution TEM (HRTEM) measurement. Visible emission spectra of NRs were measured by using a Zolix spectrophotometer (fluoroSENS 9000A) equipped with a 980 laser nm as the excitation source. The NIR-IIb emitting fluorescence was taken by using a NIR spectrometer (NIRQuest512, Ocean Optics) in the 900-1700 nm region under a 980 nm laser excitation. The fluorescence quantum yield (QY) of the PAA-NRs in water was calculated by similar method as previous report [10] by using IR-26 molecule (QY=0.5%) in 1,2-dichloroethane (DCE) as the reference system.

2.5. *In vitro* phantom NIR-IIb optical imaging

In vitro phantom NIR-IIb optical imaging of PAA-NRs solution doped with 10%Yb, 20%Yb and 30%Yb at the same concentration were captured by using a home-made short-wavelength infrared (SWIR) imaging system equipped with a InGaAs SWIR detector (Model: NIRvanaTM Camera System, Default Operating temperature: -80 °C, Princeton Instruments) with 512×640 pixels under the excitation of a 980 nm laser. Additionally, all the NIR-IIb optical imaging in this work was captured by the home-made SWIR imaging system.

2.6. Optical imaging of "HUNNU" letters

NRs solution as ink was written on paper for images of "HUNNU" letters. Optical imaging of "HUNNU" letters with/without covered by a pork slab (2 mm thickness) in NIR-I region was taken by using a multi-modal imaging system (Bruker *In Vivo* FX Pro) excited by 980 nm laser at power density of 50 mW/cm^2 and exposure time of 30 s. Additionally, NIR-IIb optical “HUNNU” imaging was acquired by using a SWIR imaging system excited by 980 nm laser at power density of 10 mW/cm^2 and exposure time of 30 ms.

2.7. *In vitro* cytotoxicity investigation

3-(4, 5-dimethylthiazol-2-yl)-2-5-diphenyl-tetrazolium bromide (MTT) assays were performed to quantify *in vitro* cytotoxicity of PAA-NRs. Human embryonic kidney 293 (Hek293) cells were seeded into a 96-well cell culture plate under 37 ℃ and 5% CO_2 in Dulbecco’s Modified Eagle Medium (DMEM) for 4 h. Different concentrations of PAA-NRs (0, 100, 200, 500 and 1000 mg/mL) were dropped into the wells. Subsequently, the cells were incubated for 24 h at 37 ℃ with 5% CO_2 and then excited by a 980 nm laser (100 mW/cm^2) at 0 s, 2 s and 30 s, respectively. The cell viability of Hek293 cells was calculated by MTT assay.

2.8. *In vivo* NIR-IIb optical bioimaging and *in vivo* long-term tracking

All animal procedures obey the rules and regulations of the Laboratory Animal Center of Hunan Normal University approved by Hunan Province. To verify the feasibility of PAA-NRs for *in vivo* optical bioimaging in NIR-IIb region, Kunming mice weighted about 20 g were anesthetized by intraperitoneal injection (with 10 wt% pentobarbital sodium aqueous solution 100 μL). PAA-NRs solution at a total dose of 150 μL (3 mg/mL) was intravenously injected into the anesthetized mice. *In vivo* NIR-IIb fluorescent bioimaging was captured at expected time intervals by using the SWIR imaging system. To further detect the distribution of PAA-NRs in living animals, the main tissues (heart, liver, spleen, lung and kidney) harvested from the post-injection mice were observed.

To evaluate the blood circulation half-life, Kunming mice (n=3) were intravenously injected with PAA-NRs through tail vein. Blood samples from the mice were collected at expected time intervals (1 min, 10 min,1 h, 3 h, 6 h, 12 h and 24 h). The retention content of PAA-NRs in the blood was determined by quantifying the Y content through inductively coupled plasma-mass spectrometry (ICP-MS). Blood circulation curve was fitted to a typical two compartment model by using bi-exponential decay function to determine blood circulation half-life.

2.9. *In vivo* NIR-IIb small tumor imaging

To obtain tumor-bearing mice, HeLa cells (1×10^6 cells/site) were implanted subcutaneously into BALB/C mice. *In vivo* optical tumor imaging was performed after implanted 6–8 days. An anesthetic HeLa tumor-bearing mouse was injected intravenously with PAA-NRs (150 μL, 3 mg/mL). *In vivo* NIR-IIb optical imaging of tumor-bearing mouse was captured at certain time intervals. After 24 h treatment, the liver, spleen and tumor were collected from the tumor-bearing mouse for *ex vivo* NIR-IIb imaging under 980 nm laser excitation.

2.10. Blood vessel imaging in NIR-IIb region

For dynamic vessel imaging of whole-body mouse in NIR-IIb region, the anesthetized mouse was intravenously injected with PAA-NRs, and then immediately be recorded for NIR-IIb optical imaging. Power density of 980 nm laser was about 100 mW/cm^2 and the exposure time of each image was 2 s. A frame rate for the video imaging was 3 frames s^{-1}. Additionally, whole-body NIR-IIb vessel imaging of a mouse after dissection treatment was also carried out. All the whole-body imaging in this work used a SWIR lens (25 mm, Edmund Optics) with a field of view of 14.6 cm×18.3 cm. For *in vivo* dynamic vessel imaging in brain, backside and abdomen of mouse, the experimental parameters were the same as the aforementioned whole-body vessel imaging excepting the SWIR lens (100 mm, Edmund Optics) with a field of view of 26 mm×21 mm.

2.11. Histological assessment

PAA-NRs solution at a total dose of 150 μL (3 mg/mL) was intravenously injected into Kunming mice via tail vein as an experiment group, and the non-treatment mouse was regarded as a control group. For histology analysis, the mice after 4 and 7 days injection and the control group were sacrificed. The tissues (heart, liver, spleen, lung and kidney) achieved from the sacrificed mice were stained with hematoxylin and eosin (H&E). Histological sections were observed by using an optical microscope.

3. Results and discussion

3.1. Phase and microstructure characterization

Fig. 1a shows non-invasive cerebral vascular imaging of a mouse model using PAA-NRs as NIR-IIb fluorescent agents. To confirm the optimal Yb dopant concentration, $NaYF_4$ NRs doped with different Yb concentrations were constructed. NRs were first identified by XRD for detecting crystal phase structure (Fig. 1b). When increasing Yb concentrations from 10% to 30%, all of the characteristic diffraction peaks of $NaYF_4$:40%Gd/xYb/2%Er NRs were matched well with the hexagonal phase structure (JCPDS: 27-1427). No other impurity peaks were detected, confirming the formation of pure hexagonal phase. TEM images presented uniform rod-like morphology of NRs even increasing the Yb concentrations up to 30%

(Fig. 1c-1e). The average lengths of $NaYF_4$ NRs with increasing Yb^{3+} contents from 10% to 30% were measured to be about 384.3 nm, 367.8 nm and 363.6 nm, respectively, indicating the negligible size change via doping Yb (10-30%) in $NaYF_4$:Gd host. A HRTEM image displayed that the synthesized rare-earth doped NRs presented high crystalline nature (Fig. S1), and the fringe spacing was measured to be about 2.975 Å, corresponding to the (100) lattice plane of the hexagonal phase $NaYF_4$. EDS analysis further confirmed the existence of Na, Y, F, Yb and Gd elements in NRs except for the detected Cu from TEM grid (Fig. S2).

3.2. Enhanced NIR-IIb emission properties

The influence of Yb dopant concentrations on optical properties of NRs was studied. Fig. 2a shows the typical emission spectra involving upconversion visible and downconversion NIR-IIb regions of NRs with Yb doping concentrations ranging from 10% to 30%. The characteristic emission peaks (Fig. 2b) located at 529, 541, 657 and 1520 nm were ascribed to $^2H_{11/2} \rightarrow {}^4I_{15/2}$, $^4S_{3/2} \rightarrow {}^4I_{15/2}$, $^4F_{9/2} \rightarrow {}^4I_{15/2}$ and $^4I_{13/2} \rightarrow {}^4I_{15/2}$ transitions of Er ions, respectively [44,54]. And NIR-IIb emission of NRs presented narrow band with band-width of 182 nm, which is narrower than SWNTs [4]. When the Yb doping concentration was increased from 10% to 20%, distinct increases in visible and NIR-IIb intensities were most likely ascribed to the enhanced energy transfer between Yb and Er. With further increasing Yb dopant concentration from 20% to 30%, reductions in the visible and NIR-IIb intensities may be attributed to the concentration quenching. Furthermore, the NIR-IIb intensity of 20%Yb doped NRs was calculated to be about 1.2 times higher than that of 10%Yb doped NRs, demonstrating an enhancement of NIR-IIb emission by adjusting Yb contents. Additionally, to further study the Yb-doping induced optical property evolution, *in vitro* phantom imaging of NRs solutions doped with different Yb concentrations was performed (inset of Fig. 2a) by using a home-made SWIR imaging system under a 980 nm laser excitation (Fig. S3), further validating the NIR-IIb optical signal of the 20%Yb doped NRs was the strongest among all the samples. After PAA modification, the NIR-IIb fluorescent intensity of PAA-NRs in water was quenched by 8.2 times (Fig. S4) than OA-NRs in cyclohexane. The fluorescence QY in the NIR-IIb region of PAA-NRs in water was measured to be about 0.994%, which was much higher than that of SWNTs probes [30,55]. Additionally, the PAA-NRs presented high photostability in water and phosphate buffered solution (PBS) with negligible decay under continuous 980 nm excitation for 2 h (Fig. S5). Therefore, the synthesized PAA-NRs with high photo-stability and high brightness nature are optimal NIR-IIb fluorescent agents.

To demonstrate the superiority of NIR-IIb emission than NIR-I, NRs solution-based ink was written on paper as “HUNNU” letters. The optical imaging in NIR-I (650 nm) and NIR-IIb (1520 nm) regions was obtained by using a 980 nm laser at power density of 50 mW/cm^2 and 10 mW/cm^2 and exposure time of 30 s and 30 ms, respectively. As shown in Fig. 2c and 2e, the signal-to-noise (S/N) ratio achieved by imaging in NIR-IIb region (S/N=168) was higher than that in NIR-I region (S/N=160). Thus, compared with upconverted NIR-I emission, downconversion NIR-IIb emission possessed higher sensitivity and efficiency for optical imaging even excited by lower power density and shorter exposure time. Additionally, the letters covered by a 2 mm pork slab for optical imaging were carried out under idential experiment parameters. As shown in Fig. 2d and 2f, the imaging of “HUNNU” letters in NIR-I window (S/N=4) was indistinct while it was still clear in NIR-IIb region (S/N =48) covered by pork tissue due to the lower scattering losses in NIR-II region than NIR-I [3,4]. Therefore, it is expected that these NIR-IIb emitting NRs were ideal probe for *in vivo* optical bioimaging with high sensitivity and resolution.

3.3. Cytotoxicity evaluation

Good bio-compatibility of nanoprobes is essential for biomedical applications. *In vitro* cytotoxicity of Hek293 cells treated with PAA-NRs was evaluated by using MTT assay. As demonstrated in Fig. S6, high cell viability (>88%) can be observed after 24 h cultivation with PAA-NRs even increasing concentration up to 1000 μg/mL, indicating low cytotoxicity of PAA-NRs *in vitro* and potential for *in vivo* biomedical applications. Additionally, to detect the cytotoxicity of PAA-NRs after receiving illumination, the cell viability of Hek293 cells cultured with PAA-NRs after excited by 980 nm laser (100 mW/cm^2) at different exposure times (2 s, 30 s) was detected. As shown in Fig. S7, the cell viability was high than 85% although the exposure time was 30 s. Therefore, the PAA-NRs present low cytotoxicity even receiving the 980 nm laser illumination.

3.4. *In vivo* real-time tracking/biodistribution and small tumor detection

In view of good bio-compatibility and high-performance NIR-IIb emission, PAA-NRs solution was intravenously injected to anesthetized mice for *in vivo* NIR-IIb optical bioimaging. As shown in Fig. 3a, a significant NIR-IIb signal from liver region can be detected at 2 h post-injection, indicating NIR-IIb emitting PAA-NRs can be applied as fluorescent nanoprobes for *in vivo* fluorescent bioimaging. Additionally, to investigate metabolic mechanism of PAA-NRs in living mice, *in vivo*/*ex vivo* NIR-IIb optical bioimaging of intravenous injection mice was carried out under 980 nm laser excitation at different time intervals. As exhibited in the top view of Fig. 3a, a NIR-IIb signal in liver region enhanced before 12 h post-injection and then gradually decreased with prolonging post-injection time. The corresponding statistical average intensity of NIR-IIb signal was shown in Fig. S8a. Apparently, the intensity of NIR-IIb signal reached to the maximum value after 12 h treatment and then was gradually weakened. In the lateral view (Fig. 3b), NIR-IIb signals can be detected not only in liver but also in spleen. The relevant average NIR-IIb signal intensity of spleen was demonstrated in Fig. S8b. When the post-injection time was 24 h, the *in vivo* NIR-IIb signal intensity of spleen was strongest and then gradually decreased. Additionally, to further investigate the accurate biodistribution, the heart, liver, spleen, lung and kidney harvested from the treated mice were used for *ex vivo* imaging detection. As shown in Fig. S9, no NIR-IIb signal can be observed in heart and kidney. Both liver and spleen presented significant NIR-IIb signals, and the corresponding mean intensity was exhibited in Fig. S10a and S10b. The *ex vivo* intensity of NIR-IIb signal of spleen and liver reached to the maximum value after 24 h and 12 h injection, respectively, and then gradually decreased, matching with the aforementioned results of *in vivo* real-time tracking. Additionally, the lung region presented a new but weak NIR-IIb fluorescent signal (Fig. S9, Fig. S10c). Therefore, PAA-NRs were mainly accumulated in reticuloendothelial system (RES), which is similar to the previous result of biodistribution of $NaYbF_4$:Tm^{3+} nanoprobes *in vivo* [56]. The decreases of NIR-IIb fluorescent signals revealed that the PAA-NRs were gradually eliminated from the body. Based on the above results, the main excretion mechanism of PAA-modified NRs may be hepatic excretion route. Moreover, the blood retention time of the PAA-NRs was investigated by ICP-MS analysis. As shown in Fig. S11, the half-life of the PAA-NRs in blood circulation was calculated to be about 75.5 mins (Fig. S11).

To confirm the potential application of NIR-IIb emitting PAA-NRs as fluorescent nanoprobes for small tumor detection, a HeLa tumor-bearing mouse was regarded as an experimental model. After intravenously injected with PAA-NRs, *in vivo* NIR-IIb optical bioimaging of HeLa tumor-bearing mouse was performed under a 980 nm laser excitation. As exhibited in Fig. 3c, only liver and spleen present NIR-IIb signals at 5 min post-injection. After 2 h treatment, a NIR-IIb signal can be detected in the HeLa tumor region. The intensity of NIR-IIb signal of tumor region was enhanced with increasing the post-injection time. Additionally, the intensities of NIR-IIb signals of liver and spleen were increased after 12 h and 24 h treatment, respectively. This result can match with the aforementioned result of *in vivo* tracking bioimaging of the normal mouse well. Fig. 3d presented the digital photograph of the HeLa tumor-bearing mouse. To make tumor imaging more visualized, the outer skin of tumor region was removed and then detected for *in vivo* optical bioimaging (Fig. 3e), indicating more clear visualization of tumor. The size of isolated tumor was measured to be about 4 mm (Fig. 3f). Additionally, the efficient NIR-IIb signal detected from *ex vivo* imaging of the isolated tumor further validated the successful accumulation of PAA-NRs probes in tumor site (Fig. 3g, Fig. S12). And the mechanism for accumulating non-targeting PAA-NRs to tumor region is mainly ascribed to the enhanced permeability and retention (EPR) effects [57,58]. These results indicate the PAA-NRs possess potential application as excellent NIR-IIb optical nanoprobes for small tumor detection.

3.5. *In vivo* fast vessel imaging

To validate the feasibility of PAA-NRs for *in vivo* fast vessel imaging, a Kunming mouse after intravenous injection with PAA-NRs was immediately carried out for dynamic vessel imaging in NIR-IIb region (Movie S1). Fig. 4a displayed the time-dependent fluorescent intensity of *in vivo* whole-body vessel imaging. A strong NIR-IIb fluorescent signal from vessel can be detected at 10 s post-injection. And the signal decreased with increasing the post-injection time and was scarcely observed after 200 s. Additionally, the blood vessel imaging was more well-defined after dissection experiment (Fig. S13a). To test the width of blood vessel, the peaks of the fluorescent intensity profiles along the colorized lines marked in Fig. S13a were identified and fitted to Gaussian functions for the value of full width at half maximum (FWHM). As shown in Fig. S13b-13d, the calculated FWHM values extracted from NIR-IIb luminescence images were of 0.44, 0.39 and 0.94 mm. These results revealed that the synthesized PAA-NRs can be applied as fluorescent agents for *in vivo* fast vessel imaging.

To further study the resolution of vessel imaging based on PAA-NRs, *in vivo* fast NIR-IIb fluorescent imaging for abdomen and backside after intravenous treatment was carried out by using InGaAs SWIR detector with a field of view of 26 mm × 21 mm and a pixel size of 41 μm in the view. Movie S2 and Movie S3 present the dynamic vessel imaging of abdomen and backside in NIR-IIb window. At vascular bifurcations (Fig. 4b and 4c), fine vessels could be distinguished obviously and lasted for about 400 s, indicating the high resolution of PAA-NRs for vessel imaging. The corresponding cross-sectional fluorescent intensity profiles across vessel bloods were characterized by sharp peaks. After fitted by Gaussian functions, the calculated FWHM values of the selected abdomen blood vessels were 408.39, 119.54 and 76.00 μm (Fig. S14c-14e), and the backside vessels were 99.48, 122.25 and 253.55 μm (Fig. S15c-15e). These results proved that smaller and higher-order branches of vessels can be clearly visualized in the NIR-IIb region at higher magnifications.

3.6. Non-invasive *in vivo* brain vessel imaging

Encouraged by the aforementioned findings, PAA-NRs solution was injected into a normal Kunming mouse and then carried out for non-invasive brain vessel imaging at a speed of 3 frames s^{-1} in NIR-IIb region (Movie S4). As shown Fig. 5a, small cerebral vessels with high resolution were distinctly observed in NIR-IIb region after 10 s treatment. The inferior cerebral vein (marked 1), the superior sagittal sinus (marked 2) and the transverse sinus (marked 3) of brain could be clearly identified from the cerebral vascular imaging. Fluorescent signal reduced significantly after 100 s post-injection, and NIR-IIb signal was almost disappeared after 300 s post-injection. Therefore, the synthesized PAA-NRs can be applied as fluorescent agents for non-invasive cerebral vascular imaging through scalp and skull without craniotomy. To evaluate the blood vessel imaging resolution, one of the cerebral images was chosen to study (Fig. 5b and 5c). The corresponding zoom-in images of the chosen zones were exhibited in Fig. 5c. Blood vessels in NIR-IIb region were identified distinctly with high spatial resolution. The cross-sectional analyses across the blood vessels were performed, and the corresponding fluorescent intensity profiles were exhibited in Fig. 5d-5g. The peaks were fitted into Gaussian functions to extract the FWHM values from the NIR-IIb imaging. The vessel widths were measured to be 84.55, 186.17 and 312.52 μm (Fig. 5d-5g). And the smallest measureable vessel with a diameter down to about only 43.65 μm can be clearly observed. It should be pointed out that the measured resolution up to 43.65 μm is nearly closed to the limit of resolution at the imaging conditions with a field of view of 26 mm × 21 mm and a pixel size of 41 μm in the view. Compared with magnetic resonance brain imaging [59], NIR-IIb optical brain imaging in this work presents higher sensitivity and quicker feedback. Therefore, the synthesized PAA-NRs in this work can be served as optimal fluorescent nanoprobes for non-invasive *in vivo* fast cerebral vessel imaging with high spatial resolution, possessing the potential application in vascular disease imaging.

3.7. Histological analysis

To further evaluate the *in vivo* toxicity of PAA-NRs, histological analyses of main organs (heart, liver, spleen, lung and kidney) from mice with/without intravenous treatment were performed. The H&E stained tissue sections were exhibited in Fig. 6. No apparent pathology changes or tissue damages were presented between the control and experimental mice (after treatment for 4 and 7 days). These evaluation results reveal that PAA-NRs present low *in vivo* toxicity and hold a great promise for biomedical applications.

4. Conclusions

In summary, PAA-NRs with high-performance NIR-IIb emission for optical-guided small tumor detection and non-invasive *in vivo* vascular vessel imaging with high spatial and temporal resolution are successfully demonstrated. The results of *in vitro* and *in vivo* toxicity tests revealed the PAA-NRs presented good bio-compatibility and low side effects for small animals. PAA-NRs can be served as optimal NIR-IIb fluorescent agents for *in vivo* optical bioimaging, and were excreted from living animal through hepatic clearance route. Additionally, PAA-NRs can be used for visualization of small malignant tumor (4 mm in diameter) by NIR-IIb optical imaging. Importantly, the dynamic imaging capability and non-invasive natures of NIR-IIb cerebral vessel imaging with high spatial (down to 43.65 μm) and high temporal resolution were achieved. Therefore, these findings reveal that the PAA-NRs are ideal NIR-IIb probes for optical imaging-guided non-invasive *in vivo* vessel imaging.

Acknowledgment

This work was supported by the National Natural Science Foundation of China (21671064), CAS/SAFEA International Partnership Program for Creative Research Teams, and Science and Technology Planning Project of Hunan Province (No. 2017RS3031).

References

[1] S.N. Wright, P. Kochunov, F. Mut, M. Bergamino, K.M. Brown, J.C. Mazziotta, et al., Digital reconstruction and morphometric analysis of human brain arterial vasculature from magnetic resonance angiography, Neuroimage 82 (2013) 170-181.

[2] N.G. Horton, K. Wang, D. Kobat, C.G. Clark, F.W. Wise, C.B. Schaffer, et al., *In vivo* three-photon microscopy of subcortical structures within an intact mouse brain, Nat. Photonics 7 (2013) 205–209.

[3] G.S. Hong, S. Diao, J.L. Chang, A.L. Antaris, C.X. Chen, B. Zhang, et al., Through-skull fluorescence imaging of the brain in a new near-infrared window, Nat. Photonics 8 (2014) 723–730.

[4] G.S. Hong, J.C. Lee, J.T. Robinson, U. Raaz, L.M. Xie, N.F. Huang, et al., Multifunctional *in vivo* vascular imaging using near-infrared II fluorescence, Nat. Med. 18 (2012) 1841–1848.

[5] P. Schramm, P.D. Schellinger, J.B. Fiebach, S. Heiland, O. Jansen, M. Knauth, et al., Comparison of CT and CT angiography source images with diffusion-weighted imaging in patients with acute stroke within 6 hours after onset, Stroke 33 (2002) 2426–2432.

[6] C. Jacoby, Y.C. Böring, A. Beck, A. Zernecke, V. Aurich, C. Weber, et al., Dynamic changes in murine vessel geometry assessed by high-resolution magnetic resonance angiography: a 9.4T study, J. Magn. Reson. Imaging 28 (2008) 637–645.

[7] J.F. Toussaint, G.M. Lamuraglia, J.F. Southern, V. Fuster, H.L. Kantor, Magnetic resonance images lipid, fibrous, calcified, hemorrhagic, and thrombotic components of human atherosclerosis *in vivo*, Circulation 94 (1996) 932–938.

[8] M.J. Paulus, S.S. Gleason, S.J. Kennel, P.R. Hunsicker, D.K. Johnson, High resolution X-ray computed tomography: an emerging tool for small animal cancer research, Neoplasia 2 (2000) 62–70.

[9] O.T. Bruns, T.S. Bischof, D.K. Harris, D. Franke, Y.X. Shi, L. Riedemann, et al., Next-generation *in vivo* optical imaging with short-wave infrared quantum dots, Nature Biomedical Engineering 1 (2017) 56–76.

[10] A.L. Antaris, H. Chen, K. Cheng, Y. Sun, G.S. Hong, C.R. Qu, et al., A small-molecule dye for NIR-II imaging, Nat. Mater. 15 (2016) 235–243.

[11] G.S. Hong, Y.P. Zou, A.L. Antaris, S. Diao, D. Wu, K. Cheng, et al., Ultrafast fluorescence imaging *in vivo* with conjugated polymer fluorophores in the second near-infrared window, Nature Commun. 5 (2014) 4206–4215.

[12] S. Diao, J.L. Blackburn, G.S. Hong, A.L. Antaris, J.L. Chang, J.Z. Wu, et al., Fluorescence imaging *in vivo* at wavelengths beyond 1500 nm, Angew. Chem. Int. Ed. 127 (2015) 14971–14975.

[13] R. Weissleder, A clearer vision for *in vivo* imaging, Nat. Biotechnol. 19 (2001) 316–317.

[14] a) J. Zhou, Z. Liu, F.Y. Li, Upconversion nanophosphors for small-animal imaging, Chem. Soc. Rev. 41 (2012) 1323–1349;

b) D.M. Yang, P.A. Ma, Z.Y. Hou, Z.Y. Cheng, C.X. Li, J. Lin, Current advances in lanthanide ion (Ln^{3+})-based upconversion nanomaterials for drug delivery, Chem. Soc. Rev. 44 (2015) 1416–1448;

c) Y.S. Liu, D.T. Tu, H.M. Zhu, X.Y. Chen, Lanthanide-doped luminescent nanoprobes: controlled synthesis, optical spectroscopy, and bioapplications, Chem. Soc. Rev. 42 (2013) 6924–6958;

d) L. Cheng, C. Wang, L.Z. Feng, K. Yang, Z. Liu, Functional nanomaterials for phototherapies of cancer, Chem. Rev. 114 (2014) 10869–10939;

e) S.J. Zeng, Z.G. Yi, W. Lu, C. Qian, H.B. Wang, L. Rao, T.M. Zeng, H.R. Liu, H.J. Liu, B. Fei, J.H. Hao, et al., Simultaneous realization of phase/size manipulation, upconversion luminescence enhancement, and blood vessel imaging in multifunctional nanoprobes through transition metal Mn^{2+} doping, Adv. Funct. Mater. 24 (2014) 4051–4059;

f) S.J. Zeng, M.K. Tsang, C.F. Chan, K.L. Wong, J.H. Hao, PEG modified $BaGdF_5$:Yb/Er nanoprobes for multi-modal upconversion fluorescent, *in vivo* X-ray computed tomography and biomagnetic imaging, Biomaterials 33 (2012) 9232–9238;

g) G.X. Bai, M.K. Tsang, J.H. Hao, Luminescent ions in advanced composite materials for multifunctional applications, Adv. Funct. Mater. 26 (2016) 6330–6350.

[15] A.N. Bashkatov, E.A. Genina, V.I. Kochubey, V.V. Tuchin, Optical properties of human skin, subcutaneous and mucous tissues in the wavelength range from 400 to 2000 nm, J. Phys. D 38 (2005) 2543–2555.

[16] Y.T. Lim, S. Kim, A. Nakayama, N.E. Stoot, M.G. Bawendi, J.V. Frangioni, Selection of quantum dot wavelengths for biomedical assays and imaging, Molecular Imaging 2 (2003) 50–64.

[17] D.J. Naczynski, M.C. Tan, M. Zevon, B. Wall, J. Kohl, A. Kulesa, et al., Rare-earth-doped biological composites as *in vivo* shortwave infrared reporters, Nat. Commun. 4 (2013) 2199–2209.

[18] I. Villa, A. Vedda, I.X. Cantarelli, M. Pedroni, F. Piccinelli, M. Bettinelli, et al., 1.3 μm emitting SrF_2: Nd^{3+} nanoparticles for high contrast *in vivo* imaging in the second biological window, Nano Res. 8 (2015) 649–665.

[19] X.Y. Jiang, C. Cao, W. Feng, F.Y. Li, Nd^{3+}-doped $LiYF_4$ nanocrystals for the bio-imaging in the second near-infrared window, J. Mater. Chem. B 4 (2016) 87–95.

[20] R. Wang, L. Zhou, W.X. Wang, X.M. Li, F. Zhang, *In vivo* gastrointestinal drug-release monitoring through second near-infrared window fluorescent bioimaging with orally delivered microcarriers, Nat Commun. 8 (2017) 14702–14714.

[21] A.L. Antaris, H. Chen, S. Diao, Z.R. Ma, Z. Zhang, S.J. Zhu, et al., A high quantum yield molecule-protein complex fluorophore for near-infrared II imaging, Nature Commun. 8 (2017) 15269–15270.

[22] Q.L. Yang, Z.R. Ma, H.S. Wang, B. Zhou, S.J. Zhu, Y.T. Zhong, et al., Rational design of molecular fluorophores for biological imaging in the NIR-II window, Adv. Mater. 29 (2017) 1605497–1605506.

[23] C. Cao, M. Xue, X.G. Zhu, P.Y. Yang, W. Feng, F.Y. Li, Energy transfer highway in Nd^{3+}-sensitized nanoparticles for efficient near-infrared bioimaging, ACS Appl. Mater. Interfaces 9 (2017) 18540–18548.

[24] S. Diao, G.S. Hong, A.L. Antaris, J.L. Blackburn, K. Cheng, Z. Cheng, et al., Biological imaging without autofluorescence in the second near-infrared region, Nano Res. 8 (2015) 3027–3035.

[25] G.S. Hong, J.T. Robinson, Y.J. Zhang, S. Diao, A.L. Antaris, Q.B. Wang, et al., *In vivo* fluorescence imaging with Ag_2S quantum dots in the second near-infrared region, Angew. Chem. Int. Ed. 124 (2012) 1–5.

[26] B.H. Dong, C.Y. Li, G.C. Chen, Y.J. Zhang, Y. Zhang, M.J. Deng, et al., Facile synthesis of highly photoluminescent Ag_2Se quantum dots as a new fluorescent probe in the second near-infrared window for *in vivo* imaging, Chem. Mater. 25 (2013) 2503–2509.

[27] Y. Zhang, G.S. Hong, Y.J. Zhang, G.C. Chen, F. Li, H.J. Dai, et al., Ag_2S quantum dot: a bright and biocompatible fluorescent nanoprobe in the second near-infrared window, ACS Nano 6 (2012) 3695–3702.

[28] Y. Zhang, Y.J. Zhang, G.S. Hong, W. He, K. Zhou, K. Yang, et al., Biodistribution, pharmacokinetics and toxicology of Ag_2S near-infrared quantum dots in mice, Biomaterials 34 (2013) 3639–3646.

[29] C.N. Zhu, P. Jiang, Z.L. Zhang, D.L. Zhu, Z.Q. Tian, D.W. Pang, Ag_2Se quantum dots with tunable emission in the second near-infrared window, ACS Appl. Mater. Interfaces 5 (2013) 1186–1189.

[30] K. Welsher, Z. Liu, S.P. Sherlock, J.T. Robinson, Z. Chen, D. Daranciang, et al., A route to brightly fluorescent carbon nanotubes for near-infrared imaging in mice, Nat. Nanotechnol. 4 (2009) 773–780.

[31] J.T. Robinson, G.S. Hong, Y.Y. Liang, B. Zhang, O.K. Yaghi, H.J. Dai, *In vivo* fluorescence imaging in the second near-infrared window with long circulating carbon nanotubes capable of ultrahigh tumor uptake, J. Am. Chem. Soc. 134 (2012) 10664–10669.

[32] K. Welsher, S.P. Sherlock, H.J. Dai, Deep-tissue anatomical imaging of mice using carbon nanotube fluorophores in the second near-infrared window, PNAS 108 (2011) 8943–8948.

[33] Z. M. Tao, G.S. Hong, C. Shinji, C.X. Chen, S. Diao, A.L. Antaris, et al., Biological imaging using nanoparticles of small organic molecules with fluorescence emission at wavelengths longer than 1000 nm, Angew. Chem. Int. Ed. 52 (2013)13002–13006.

[34] B.L. Wehrenberg, C. Wang, P. Guyot-Sionnest, Interband and intraband optical studies of PbSe colloidal quantum dots, J. Phys. Chem. B 106 (2002) 10634–10640.

[35] L. Bakueva, I. Gorelikov, S. Musikhin, X.S. Zhao, E.H. Sargent, E. Kumacheva, PbS quantum dots with stable efficient luminescence in the near-IR spectral range, Adv. Mater 16 (2004) 926–929.

[36] M.T. Harrison, S.V. Kershaw, M.G. Burt, A. Eychmuller, H. Weller, A.L. Rogach, Wet chemical synthesis and spectroscopic study of CdHgTe nanocrystals with strong near-infrared luminescence, Mater. Sci. Eng. B 69 (2000) 355–360.

[37] Z. Liu, W.B. Cai, L.N. He, N. Nakayama, K. Chen, X.M. Sun, et al., *In vivo* biodistribution and highly efficient tumour targeting of carbon nanotubes in mice, Nature Nanotech. 2 (2007) 47–52.

[38] S.D. Perrault, C. Walkey, T. Jennings, H.C. Fischer, W.C.W. Chan, Mediating tumor targeting efficiency of nanoparticles through design, Nano Lett. 9 (2009) 1909–1915.

[39] a) F. Wang, X.G. Liu, Upconversion multicolor fine-tuning: visible to near-infrared emission from lanthanide-doped $NaYF_4$ nanoparticles, J. Am. Chem. Soc. 130 (2008) 5642–5643;

b) D.L. Ni, W.B. Bu, S.J. Zhang, X.P. Zheng, M. Li, H.Y. Xing, et al., Single Ho^{3+}-doped upconversion nanoparticles for high-performance T_2-weighted brain tumor diagnosis and MR/UCL/CT multimodal imaging, Adv. Funct. Mater. 24 (2014) 6613–6620;

c) Z.L. Xue, Z.G. Yi, X.L. Li, Y.B. Li, M.Y. Jiang, H.R. Liu, et al., Upconversion optical/magnetic resonance imaging-guided small tumor detection and *in vivo* tri-modal bioimaging based on high-performance luminescent nanorods. Biomaterials 115 (2017) 90–103;

d) Z.G. Yi, X.L. Li, Z.L. Xue, X. Liang, W. Lu, H. Peng, et al., Remarkable NIR enhancement of multifunctional nanoprobes for *in vivo* trimodal bioimaging and upconversion optical/T_2-weighted MRI-guided small tumor diagnosis, Adv. Funct. Mater. 25 (2015) 7119–7129.

[40] R. Wang, F. Zhang, NIR luminescent nanomaterials for biomedical imaging, J. Mater. Chem. B 2 (2014) 2422–2443.

[41] X.N. Dang, L. Gua, J.F. Qi, S. Correa, G. Zhang, A.M. Belchera, et al., Layer-by-layer assembled fluorescent probes in the second near-infrared window for systemic delivery and detection of ovarian cancer, Proc. Natl Acad. Sci. USA 113 (2016) 5179–5184.

[42] W. Zheng, P. Huang, D.T. Tu, E. Ma, H.M. Zhu, X.Y. Chen, Lanthanide-doped upconversion nano-bioprobes: electronic structures, optical properties, and biodetection, Chem. Soc. Rev. 44 (2015) 1379-1415.

[43] P. Huang, W. Zheng, S.Y. Zhou, D.T. Tu, Z. Chen, H.M. Zhu, et al., Lanthanide-doped $LiLuF_4$ upconversion nanoprobes for the detection of disease biomarkers, Angew. Chem. Int. Ed. 53 (2014) 1252-1257.

[44] R. Wang, X.M. Li, L. Zhou, F. Zhang, Epitaxial seeded growth of rare-earth nanocrystals with efficient 800 nm near-infrared to 1525 nm short-wavelength infrared downconversion photoluminescence for *in vivo* bioimaging, Angew. Chem. Int. Ed. 53 (2014) 12086–12090.

[45] J.C. Boyer, F. C.J.M. van Veggel, Absolute qantum yield measurements of colloidal $NaYF_4$: Er^{3+}, Yb^{3+} upconverting nanoparticles, Nanoscale 2 (2010) 1417–1419.

[46] E. Hemmer, A. Benayas, F. Légaré, F. Vetrone, Exploiting the biological windows: current perspectives on fluorescent bioprobes emitting above 1000 nm, Nanoscale Horiz. 1 (2016) 168–184.

[47] D. Jaque, C. Richard, B. Viana, K. Soga, X.G. Liu, J.G. Solé, Inorganic nanoparticles for optical bioimaging, Adv. Opt. Photonics 8 (2016) 1–103.

[48] D.J. Naczynski, M.C. Tan, R.E. Riman, P.V. Moghe, Rare earth nanoprobes for functional biomolecular imaging and theranostics, J. Mater. Chem. B 2 (2014) 2958–2973.

[49] E. Hemmer, N. Venkatachalam, H. Hyodo, A. Hattori, Y. Ebina, H. Kishimoto, et al., Upconverting and NIR emitting rare earth based nanostructures for NIR-bioimaging, Nanoscale 5 (2013) 11339–11361.

[50] M. Kamimura, T. Matsumoto, S. Suyari, M. Umezawaab, K. Soga, Ratiometric near-infrared fluorescence nanothermometry in the OTN-NIR (NIR II/III) biological window based on rare-earth doped β-$NaYF_4$ nanoparticles, J. Mater. Chem. B 5 (2017) 1917–1925.

[51] Y.T. Zhong, Z.R. Ma, S.J. Zhu, J.Y. Yue, M.X. Zhang, A.L. Antaris, et al., Boosting the down-shifting luminescence of rare-earth nanocrystals for biological imaging beyond 1500 nm, Nature Commun. 8 (2017) 737-743.

[52] F. Wang, Y. Han, C.S. Lim, Y.H. Lu, J. Wang, J. Xu, et al., Simultaneous phase and size control of upconversion nanocrystals through lanthanide doping, Nature 463 (2010) 1061–1065.

[53] T.R. Zhang, J.P. Ge, Y.X. Hu, Y.D. Yin, General approach for transferring hydrophobic nanocrystals into water, Nano Lett. 7 (2007) 3203–3207.

[54] H.B. Wang, W. Lu, T.M. Zeng, Z.G. Yi, L. Rao, H.R. Liu, et al., Multi-functional $NaErF_4$:Yb nanorods: enhanced red upconversion emission, *in vitro* cell, *in vivo* X-ray, and T_2-weighted magnetic resonance imaging, Nanoscale 6 (2014) 2855–2860.

[55] G.S. Hong, A. L. Antaris, H. J. Dai, Near-infrared fluorophores for biomedical imaging, Nat. Biomed. Eng. 1 (2017), 0010.

[56] H.Y. Xing, W.B. Bu, Q.G. Ren, X.P. Zheng, M. Li, S.J. Zhang, et al., A $NaYbF_4$: Tm^{3+} nanoprobe for CT and NIR-to-NIR fluorescent bimodal imaging, Biomaterials 33 (2012) 5384–5393.

[57] B. K. Park, S. Lee, E. Kang, K. Kim, K. Choi, I.C. Kwon, New generation of multifunctional nanoparticles for cancer imaging and therapy, Adv. Funct. Mater. 19 (2009), 1553-1566.

[58] M. Gao, F.B. Yu, C.J. Lv, J. Choo, L.X. Chen, Fluorescent chemical probes for accurate tumor diagnosis and targeting therapy**,** Chem. Soc. Rev. 46(2017)**,** 2237-2271.

[59] M.F. Callaghan, P. Freund, B. Draganski, E. Anderson, M. Cappelletti, R. Chowdhury, et al., Widespread age-related differences in the human brain microstructure revealed by quantitative magnetic resonance imaging, Neurobiology of Aging 35 (2014) 1862–1872.

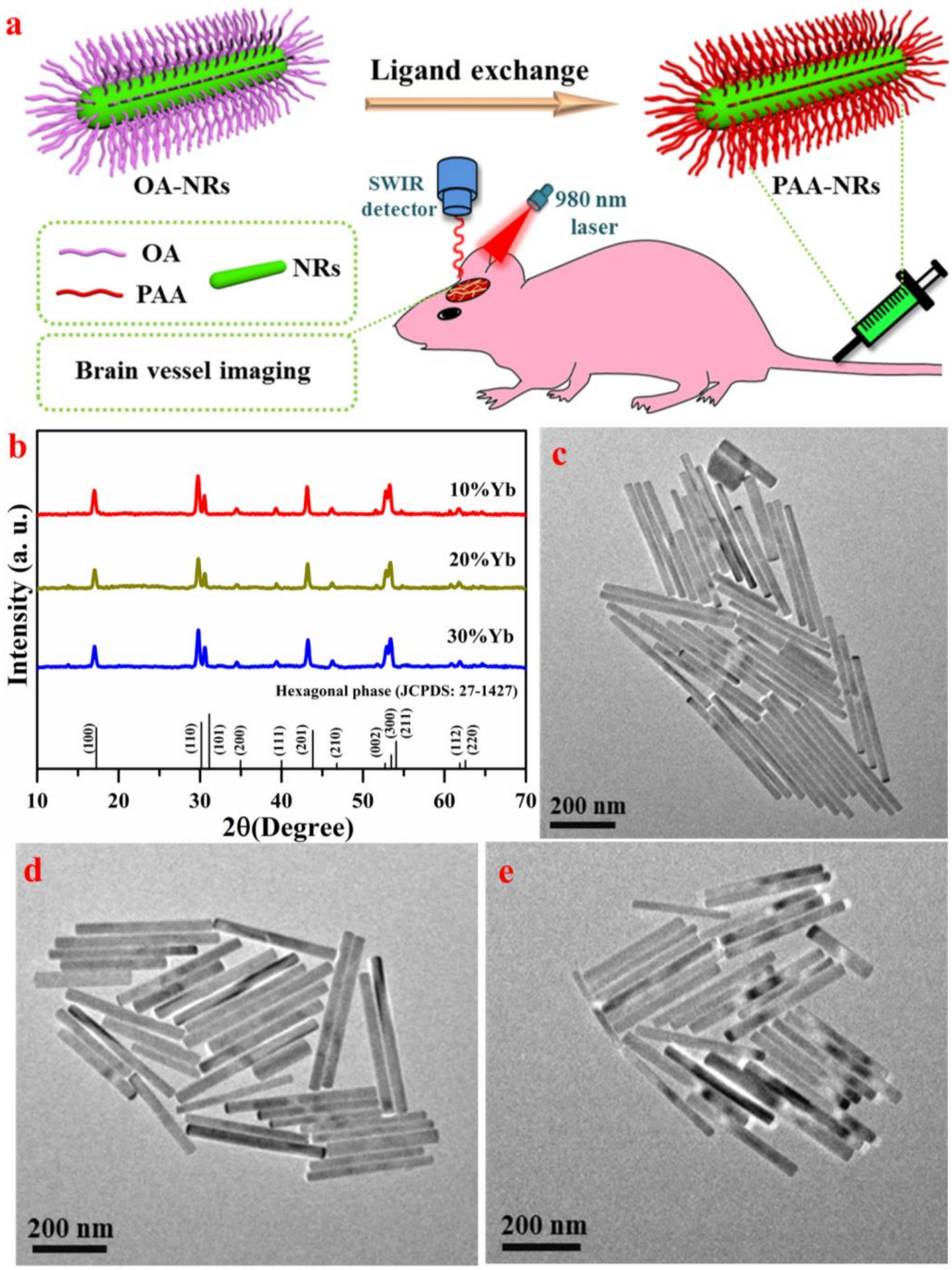

Fig. 1. a) Schematic illustration of PAA-NRs for non-invasive cerebral vessel imaging. b) XRD patterns of NRs doped with 10%Yb, 20%Yb and 30%Yb, black lines present the standard hexagonal phase (JCPDS: 27-1427). c)-e) TEM images of $NaYF_4$ NRs doped with 10%Yb, 20%Yb and 30%Yb, respectively.

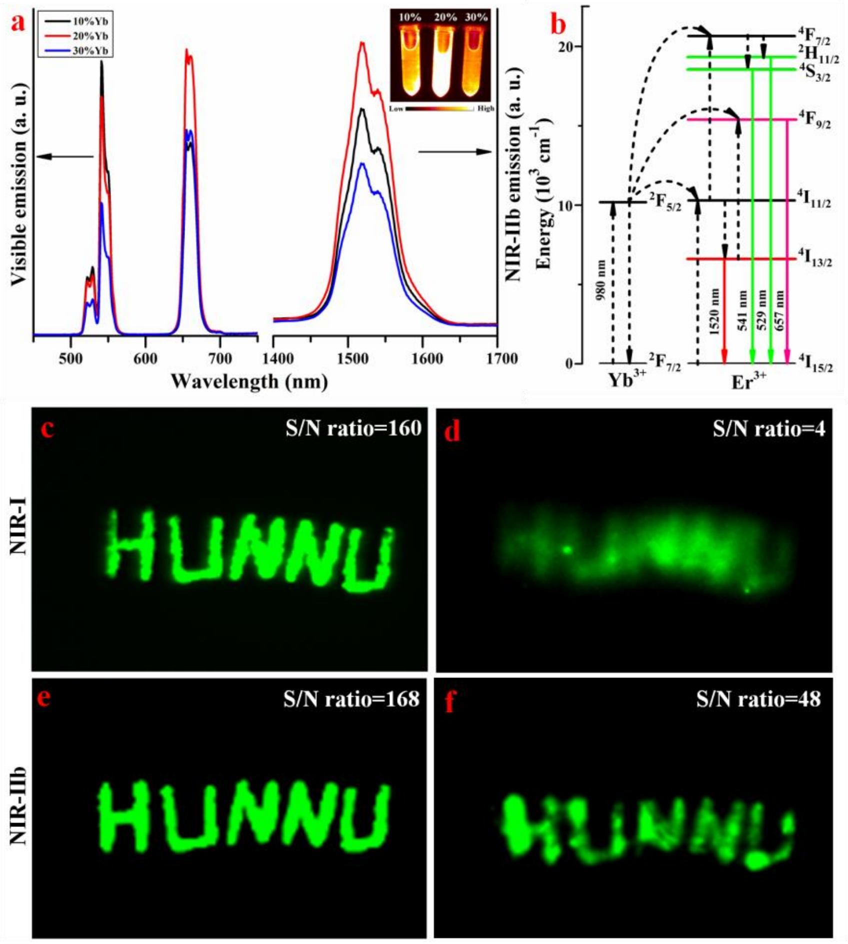

Fig. 2. a) Photoluminescence spectra of NRs spanning the visible (left) and NIR-IIb (right) regions under the excitation of 980 nm laser, inset: *in vitro* phantom NIR-IIb fluorescent imaging of PAA-NRs solution doped with different Yb^{3+} concentrations under a 980 nm laser excitation. b) Energy level diagram of $NaYF_4$:Gd/Yb/Er NRs. c) and d) fluorescent imaging of "HUNNU" letters without and with covering by a 2 mm pork slab in NIR-I red region under 980 nm laser excitation, respectively. e) and f) fluorescent imaging of "HUNNU" letters without and with covering by a 2 mm pork slab in NIR-IIb region under 980 nm laser excitation, respectively. Power density and exposure time of 980 nm laser used in NIR-I imaging were 50 mW/cm^2 and 30 s, and in NIR-IIb imaging were 10 mW/cm^2 and 30 ms, respectively.

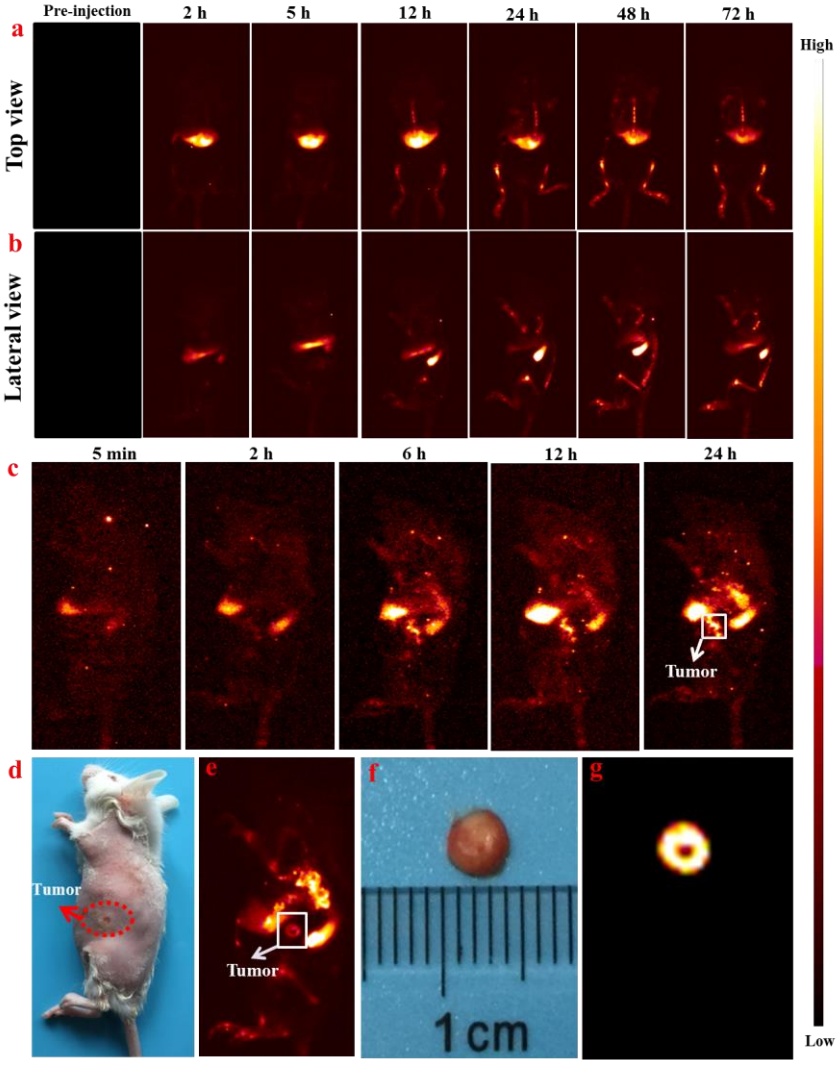

Fig. 3. a) Top view and b) lateral view of *in vivo* NIR-IIb imaging and real-time tracking of mice after intravenous injection with PAA-NRs at different time intervals under 980 nm excitation. c) NIR-IIb tumor imaging of a HeLa tumor-bearing mouse after intravenous injection of PAA-NRs at different post-injection times under a 980 nm laser excitation. d) A digital photograph of the HeLa tumor-bearing mouse, the red dotted oval indicates the HeLa tumor region. e) NIR-IIb tumor imaging of mouse after removed the skin of tumor region. f) The digital photograph of the isolated tumor and g) *ex vivo* NIR-IIb imaging of the isolated HeLa tumor.

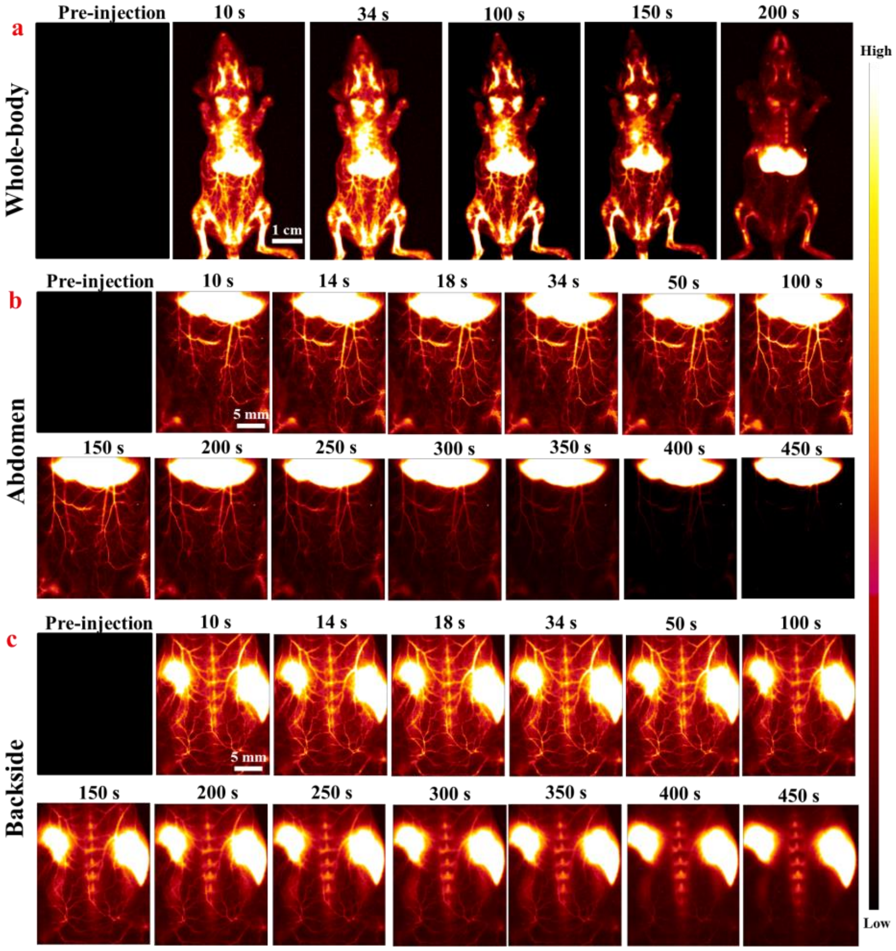

Fig. 4. *In vivo* NIR-IIb optical vessel imaging of a) whole-body, b) abdomen, c) backside of mice after intravenous injection with PAA-NRs under a 980 nm laser excitation at expected time intervals. Whole-body vessel imaging was taken by using a SWIR lens with a field of view of 14.6 cm × 18.3 cm, abdomen/backside vessel imaging of mouse was performed by a SWIR lens with a field of view of 26 mm × 21 mm.

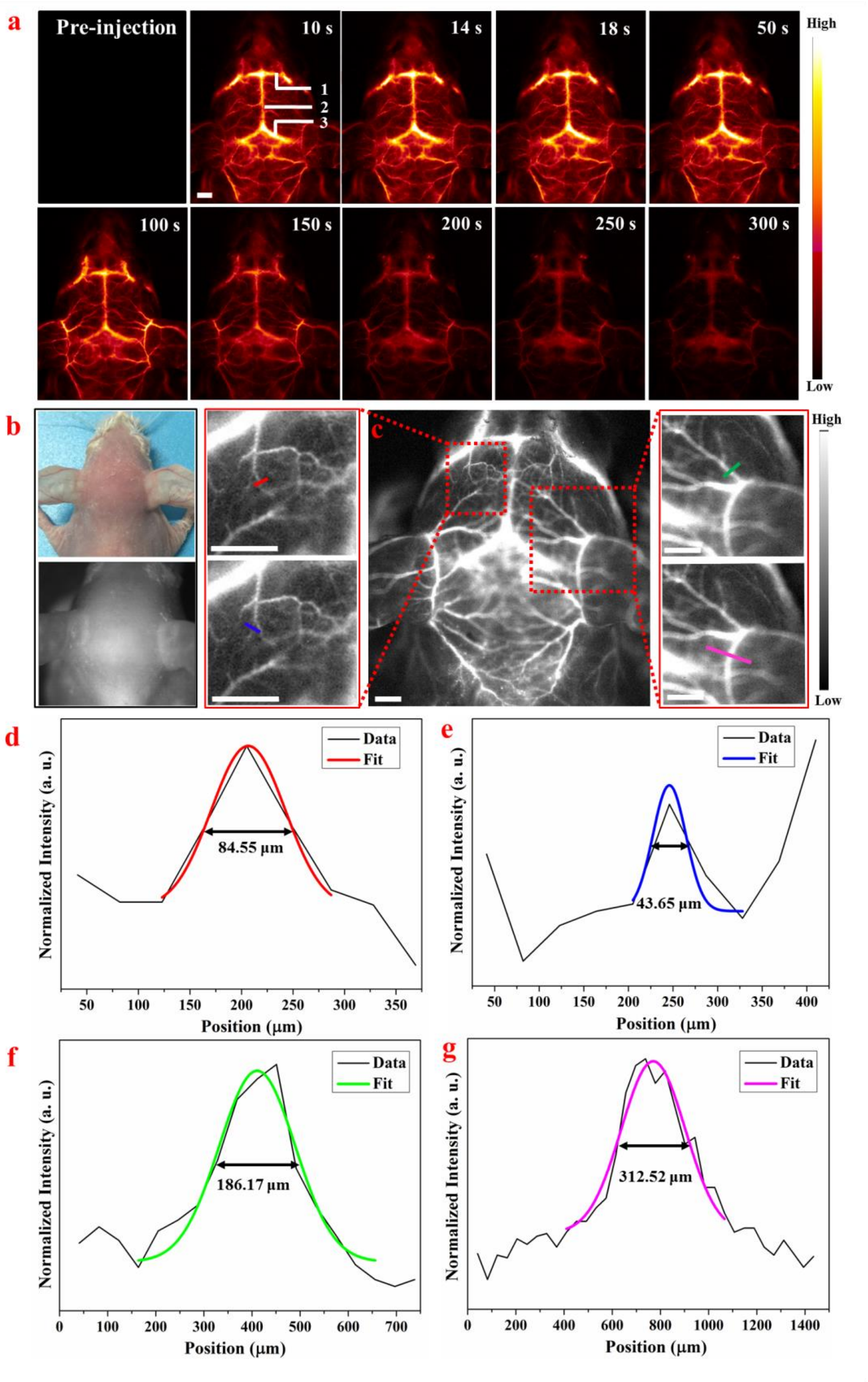
a
Pre-injection
10 s
14 s
18 s
50 s
100 s
150 s
200 s
250 s
300 s
1
2
3
High
Low
b
c
High
Low
d
Data
Fit
84.55 μm
Normalized Intensity (a. u.)
Position (μm)
50 100 150 200 250 300 350
e
Data
Fit
43.65 μm
Normalized Intensity (a. u.)
Position (μm)
50 100 150 200 250 300 350 400
f
Data
Fit
186.17 μm
Normalized Intensity (a. u.)
Position (μm)
0 100 200 300 400 500 600 700
g
Data
Fit
312.52 μm
Normalized Intensity (a. u.)
Position (μm)
0 200 400 600 800 1000 1200 1400

Fig. 5. *In-situ* non-invasive brain imaging taken by using InGaAs SWIR detector with a field of view of 26 mm×21 mm and the SWIR lens (100 mm, Edmund Optics) with a pixel size of 41 μm in the view. a) Time course NIR-IIb optical brain images taken immediately after intravenous treatment with PAA-NRs via tail vein. The 1, 2 and 3 marked in imaging presented the inferior cerebral vein, superior sagittal sinus and transverse sinus, respectively. b) A digital photograph (up) and a bright field image (bottom) of a mouse head with hair shaved off. c) A cerebral vascular image and the corresponding zoom-in images of the chosen vessels. d)-g) Cross-sectional intensity profiles (black curves), Gaussian functional fitting lines (colorized curves) and FWHM values measured along the colorized lines from the image of (c). Scale bars: 2 mm.

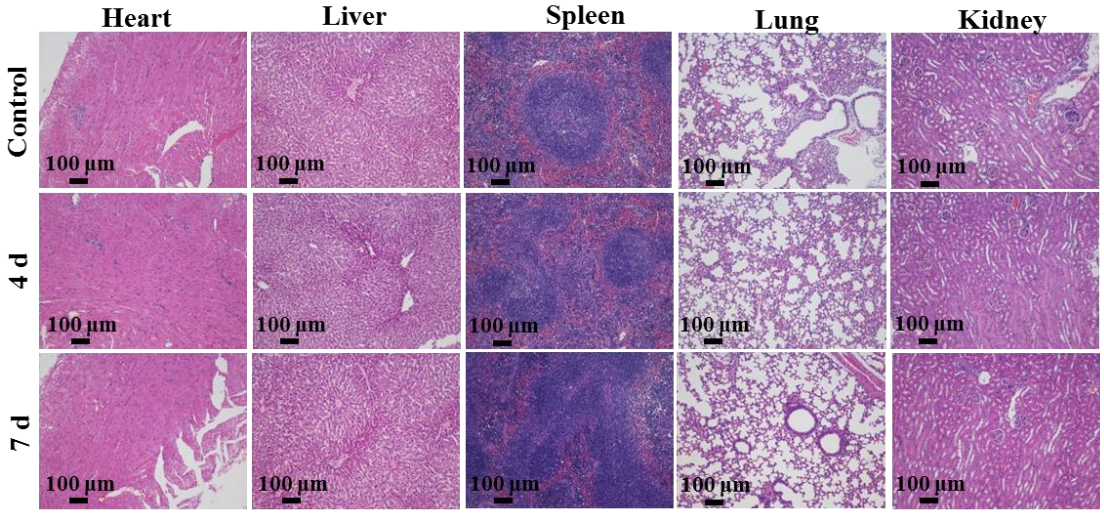

Fig. 6. H&E stained main tissues collected from control mouse and mice treated with PAA-NRs for 4 and 7 days.